Theoretical Analysis of Thermal Transport in Graphene Supported on Hexagonal Boron Nitride: The Importance of Strong Adhesion Due to π-Bond Polarization

Alexander J. Pak and Gyeong S. Hwang

Theoretical Analysis of Thermal Transport in Graphene Supported on Hexagonal Boron Nitride: The Importance of Strong Adhesion due to π-bond Polarization

Alexander J. Pak and Gyeong S. Hwang[#]

McKetta Department of Chemical Engineering, University of Texas, Austin, Texas 78712, USA

Abstract

One important attribute of graphene that makes it attractive for high-performance electronics is its inherently large thermal conductivity (κ) for the purposes of thermal management. Using a combined density functional theory and classical molecular dynamics approach, we predict that the κ of graphene supported on hexagonal boron nitride (h-BN) can be as large as 90% of the κ of suspended graphene, in contrast to the significant suppression of κ (more than 70% reduction) on amorphous silica. Interestingly, we find that this enhanced thermal transport is largely attributed to increased lifetimes of the in-plane acoustic phonon modes, which is a notable contrast from the dominant contribution of out-of-plane acoustic modes in suspended graphene. This is possible due to the charge polarization throughout graphene that induces strong interlayer adhesion between graphene and h-BN. These findings highlight the potential benefit of layered dielectric substrates such as h-BN for graphene-based thermal management, in addition to their electronic advantages. Furthermore, our study brings attention to the importance of understanding the interlayer interactions of graphene with layered dielectric materials which may offer an alternative technological platform for substrates in electronics.

[#]Author to whom correspondence should be addressed: e-mail: gshwang@che.utexas.edu

Introduction

Owing to its large electrical and thermal conductivity, graphene has been extensively explored as an active channel material in nano-scale and flexible electronics [1]. In this context, these two-dimensional sheets are typically supported on or encased in electrically insulating substrates. Recently, few-layer hexagonal boron nitride (h-BN) has been tested for its suitability as a dielectric substrate; the small lattice mismatch and atomically smooth surface of h-BN results in carrier mobilities that are an order of magnitude larger than that of conventional SiO_2 substrates [2]. Few-layer h-BN stacks have also been proposed as a means to improve heat management, thereby mitigating degradation of the substrate from local heating and enhancing overall device performance [3]. Ideally, such vertically-stacked van der Waals (vdW) heterostructures can be used to maximize the thermal anisotropy by promoting basal (*i.e.*, in-plane) thermal conductivity (κ) while minimizing the interfacial (*i.e.*, cross-plane) thermal conductance (G). To achieve this goal, it is imperative to explore the fundamental mechanisms of both in-plane and cross-plane thermal transport at these interfaces. However, only a limited number of experimental [4] and theoretical [5,6] studies have reported on the thermal transport at graphene and h-BN interfaces with their primary focus on G.

To investigate the κ and G of supported graphene, we advocate the use of molecular simulations to develop atomic-level insights. The increasingly powerful capabilities of classical molecular dynamics (MD) simulations have encouraged their use for interfacial thermal transport investigations. While much of the earlier theoretical work that focused on understanding the thermal transport physics of graphene relied on first-principles calculations based on density functional theory [7,8] (DFT), the use of classical force fields has recently been demonstrated to reproduce comparable results with experimental data [9]. These force fields enable the direct calculation of κ and G from MD simulations which can also implicitly incorporate temperature-dependent and full anharmonicity [10]. MD simulations are also useful for the study of disordered systems such as graphene supported on amorphous SiO_2 (a-SiO_2) which require system sizes that are computationally burdensome for DFT-based calculations. For example, a recent study by our group revealed that the κ of a-SiO_2-supported graphene tends to scale directly with the contact force distribution (*i.e.*, the variance of the vdW forces), which is sensitive to the morphology at the interface. Therefore, these simulations must incorporate accurate representations of the interfacial energetics.

A central aspect of layered materials is the combination of dispersion forces, electrostatic interactions, and Pauli repulsions that dictate the interlayer interactions [11]. The case of graphene supported on h-BN is particularly interesting as the polar nature of the B-N bond can induce electronic polarization throughout the graphene sheet [12,13]. Therefore, the framework of this work is as follows. We first investigate the nature of the graphene/h-BN interfacial interactions using dispersion-corrected DFT (DFT-D2). We then explore the κ and G of various graphene/h-BN heterostructures, as shown in Figure 1, based on MD simulations using the Mie potential with parameters we have optimized. Our results show that the κ (and G) of supported graphene can be enhanced (diminished) by increasing the number of h-BN support layers. Our analysis attributes this behavior to the reduced strain within graphene and increased in-plane phonon lifetimes, which is possible due to the strong interlayer adhesion between graphene and h-BN. These findings highlight the possibility of significantly improving the thermal conductivity of graphene and may prove useful for the study of other layered materials.
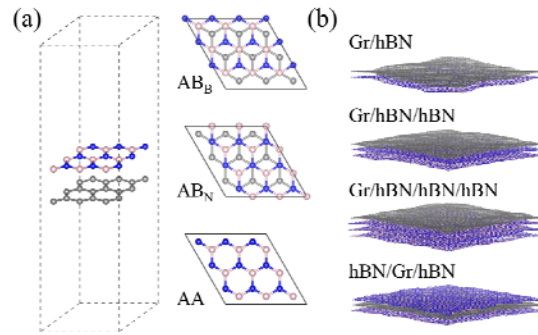

Figure 1. (a) Schematic of the simulation cell used in DFT calculations and representations of the three stacking orientations. (b) Schematic of the graphene (Gr) and hexagonal boron nitride (h-BN) heterostructures used in MD simulations. Grey, pink, and blue balls represent C, B, and N atoms, respectively.

Interlayer Interactions between Graphene and h-BN

We first investigate the nature of the interlayer interactions between monolayer graphene and h-BN using vdW-corrected DFT calculations. As shown in Figure 1(a), we consider three possible stacking configurations: AB_B, AB_N, and AA; in the former two cases, the subscript denotes the h-BN sub-lattice that is eclipsed by C while in the last case, both sub-lattices are eclipsed.

The charge density difference plots in Figure 2 show that in each case, the two C sub-lattices experience a noticeable charge redistribution as a result of interactions with the B and N sub-lattices. Previous studies [12,14] have shown that the so-called symmetry breaking resulting from sub-lattice polarization is responsible for the observed band gap opening in supported graphene. We focus on the AB_N orientation shown in Fig. 2(a) as this is the most energetically favorable configuration (as discussed below). Our DFT-D2 calculations reveal that the C sub-lattice directly adjacent to the B sub-lattice tends to accumulate electron density. On the other hand, the C sub-lattice that is staggered with the N sub-lattice exhibits laterally broadened electron depletion. With this polarization of the graphene π system, the optimal separation distance from h-BN is 3.1 Å. However, in the AB_N (Fig. 2b) and AA (Fig. 2c) configurations, the electron density tends to be vertically polarized rather than laterally broadened while the predicted separation distances are 3.3 and 3.4 Å, respectively. Upon the addition of a second h-BN layer, our calculations (Fig. S1 [15]) show that the charge density redistribution throughout graphene remains qualitatively the same as in Fig. 2 which suggests that increasing the number of h-BN layers does not noticeably affect the polarization of graphene.
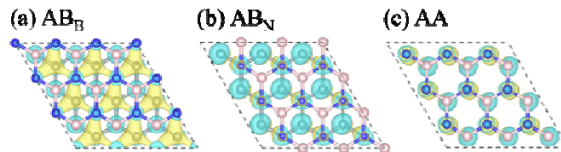

(a) AB_B (b) AB_N (c) AA

Figure 2. Charge density difference plots for monolayer h-BN/graphene for (a) AA and (b) AB_B stacking orientations. The pink, blue, and grey balls denote B, N, and C atoms, respectively. The yellow (blue) shaded regions depict isosurfaces with positive (negative) charge at a value of 0.0002 e/bohr^3. Energetically optimal separation distances between h-BN and graphene were used in each case (around 3.4 and 3.1 Å, respectively).
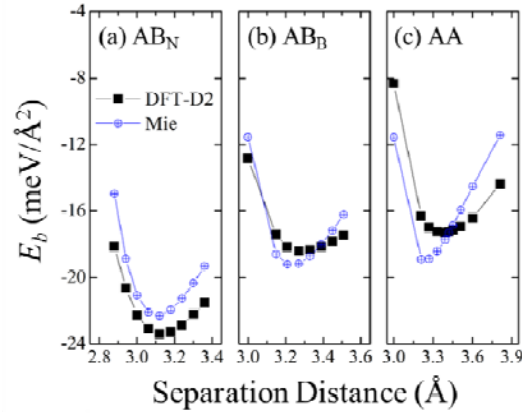
Figure 3. Comparison of the computed interlayer binding energy (E_b) at varying interlayer distances for (a) AB_B, (b), AB_N, and (c) AA orientations using DFT-D2 (black squares) and optimized Mie parameters from this work (blue open circles).

Next, we compute the interfacial binding energy (E_b) using DFT-D2 as presented in Figure 3 (see Methods). In the AB_B configuration, E_b can be as large as 23.4 meV/Å^2, which is comparatively larger than that of bilayer graphene (18.7 meV/Å^2 using DFT-D2). Another insightful comparison is to that of graphene on Cu(111), a substrate commonly used for CVD growth of graphene, which has an experimentally measured adhesion energy of 30-32 meV/Å^2 [16,17] and a DFT-D2 calculated E_b of 30.1 meV/Å^2. The large adhesion energy between graphene and Cu is likely attributed to a charge-transfer-induced short-range electrostatic interaction while the graphene p_z and Cu d_{z2} orbitals exhibit weak coupling [18]. Similarly, the combination of charge polarization and lattice matching between the graphene and h-BN sheets can result in a larger E_b with respect to bilayer graphene. We should also note that E_b is strongly orientation-dependent and can reduce by up to 40% in the AA or AB_N configurations. However, previous theoretical results [19,20] on graphene and h-BN bilayers have found that the sliding barrier between orientations is at least an order of magnitude smaller than the estimated E_b. Upon thermal annealing, we can therefore expect the graphene sheet to slide into the most favorable AB_N configuration. Another interesting comparison is to that of bilayer h-BN. In the AA' configuration in which B of the first layer is adjacent to N of the second layer, the predicted E_b is 24.1 meV/Å^2. This is marginally stronger than that of the graphene/h-BN interface, which we can expect as the interlayer B and N atoms have correspondingly stronger electrostatic attractions.

To describe E_b, we adopt the Mie potential (see Methods) and optimize the parameters in order to agree with our DFT-D2 results (Fig. 3); the optimized parameters can be found in Table 1. The Mie potential is a generalized Lennard Jones (LJ) potential that allows for fine-tuning of the interatomic attractive and repulsive contributions using the following equation:

$$E_b = \sum_{i,j>i} \left(\frac{n_{rep}}{n_{rep}-n_{att}}\right) \left(\frac{n_{rep}}{n_{att}}\right)^{\left(\frac{n_{att}}{n_{rep}-n_{att}}\right)} \varepsilon \left[\left(\frac{\sigma}{r_{ij}}\right)^{n_{rep}} - \left(\frac{\sigma}{r_{ij}}\right)^{n_{att}}\right] \tag{1}$$

where ε is the well-depth, σ is the zero-energy distance, r_{ij} is the distance between atoms i and j, n_{rep} is the exponent of the repulsive term, and n_{att} is the exponent of the attractive term. Note that when $n_{rep} = 12$ and $n_{att} = 6$, the Mie potential reduces to the 12-6 LJ potential; however, we find that the 12-6 LJ potential does not suitably describe the energetics that distinguish the three stacking orientations (Fig. S2 [15]). Herein, we will use our optimized Mie parameters to describe the graphene/h-BN interlayer interactions; the intralayer interactions for graphene and h-BN are described using optimized Tersoff potentials from Ref. [9] and [21], respectively, while the h-BN/h-BN interlayer interactions are described using a LJ potential from Ref. [22]; the π-bond polarization tends to minimally affect the interatomic forces acting on each atom in graphene (Fig. S3 [15]). In the next section, we investigate the structure and thermal transport behavior of graphene at the heterostructure interface using classical molecular dynamics (MD) simulations as described below.

Table 1. Optimized Mie parameters fit to DFT-D2 calculations to describe the Gr/h-BN interlayer interaction energy.

	ε, meV	σ, Å	n_{rep}	n_{att}
C-B	3.6	2.2132	10.38	3.58
C-N	9.0	3.2222	14.85	9.84

Interfacial Structure and Energetics

We consider four cases, as depicted in Figure 1(b), in which graphene is supported on monolayer h-BN, bilayer h-BN, trilayer h-BN, and encapsulated between two h-BN monolayers, hereafter denoted as Gr/hBN, Gr/hBN/hBN, Gr/hBN/hBN/hBN, and hBN/Gr/hBN, respectively.

First, it is informative to gauge the change in the sheet corrugation, which is defined as the standard deviation of the atomic height distribution (σ_h), with different h-BN

heterostructures. As seen in Table 2, σ_h(Gr) and σ_h(h-BN) are nearly identical as the graphene sheet tends to be well-conformed to the h-BN sheet due to the similarity of their lattice constants. Note that in every case, σ_h(Gr) is found to be consistently smaller than σ_h(h-BN) since graphene sheets tend to have larger flexural rigidity [23]. As the number of h-BN support layers increases, both σ_h(Gr) and σ_h(h-BN) are increasingly reduced. This is possible since the additional h-BN layers suppress the fluctuations throughout the h-BN stack due to the strong h-BN/h-BN interlayer interaction, which subsequently promotes a flatter graphene sheet. Interestingly, the C-B and C-N pair distribution functions (Fig. S4 [15]) reveal that the suppression in corrugation is commensurate with the graphene/h-BN stacking adopting a more AB_B-like configuration. Likewise, the h-BN layers adopt a more AA'-like configuration with the addition of layers.

Table 2. Average corrugation of graphene/adjacent h-BN (σ_h(Gr)/σ_h(h-BN)) sheets and the standard deviation of the graphene internal strain force ($\sigma|f_{st}|$) and interfacial adhesion force ($\sigma|f_{ad}|$).

	σ_h(Gr) / σ_h(h-BN) (Å)	$\sigma|f_{st}|$ (meV/Å)	$\sigma|f_{ad}|$ (meV/Å)	Sum
Gr/hBN	0.456 / 0.459	20.1	26.9	47.0
Gr/hBN/hBN	0.451 / 0.453	18.6	27.1	45.7
Gr/hBN/hBN/hBN	0.355 / 0.357	14.6	27.0	41.6
hBN/Gr/hBN	0.304 / 0.309	6.6	43.9	50.5

The sheet corrugation provides valuable insight into the distribution of the atomic forces throughout the graphene sheet, which in turn can provide insight into the thermal transport behavior. In this case, we consider the standard deviation of the adhesion force ($\sigma|f_{ad}|$), which results from the graphene/h-BN interlayer interactions, and the standard deviation of the strain force throughout graphene ($\sigma|f_{st}|$), which is driven by the C-C bonding forces. Table 2 shows that the $\sigma|f_{ad}|$ is not particularly sensitive to the small reduction in sheet corrugation as the already excellent lattice registry does not significantly change upon the addition of h-BN layers. Recall that the excellent lattice registry is possible due to the polarization-driven interlayer adhesion between graphene and h-BN. However, $\sigma|f_{ad}|$ does increase by 60% once graphene is encapsulated between monolayer h-BN sheets (*i.e.*, the hBN/Gr/hBN case) as the interlayer interactions now influence both sides. On the other hand, $\sigma|f_{st}|$ is computed to decrease with the number of h-BN layers (and encapsulation) which is consistent with the graphene sheet

becoming increasingly flat (*i.e.*, smaller σ_h(Gr)). Combining the two contributions, we estimate that the overall variation of the force distribution increases with the following trend: Gr/hBN/hBN/hBN < Gr/hBN/hBN < Gr/hBN < hBN/Gr/hBN.

Anisotropic Thermal Transport

In this section, we investigate the relationship between the interfacial structure and the in-plane κ and cross-plane thermal conductance (G) of graphene supported on h-BN at 300 K using reverse non-equilibrium MD and the thermal relaxation method, respectively (see Methods).

To establish a basis for comparison, we first calculate the κ of free-standing graphene. Given that the distance between the simulated heat source and sink ($L_{\Delta ss}$) is less than the experimentally estimated mean free path of graphene ($l_{MFP} \sim 775$ nm) [24], it is necessary to account for possible phonon boundary scattering in our prediction of κ using the following model based on the 1D kinetic theory of lattices and Matthiessen's rule:

$$\kappa = C_v v_p l_{eff} \tag{2}$$

$$l_{eff} = \left(\frac{1}{l_{MFP}} + \frac{2}{L_{\Delta ss}} \right)^{-1} \tag{3}$$

$$\frac{1}{\kappa} = \frac{2}{C_v v_p} \frac{1}{L_{\Delta ss}} + \frac{1}{C_v v_p l_{MFP}} \tag{4}$$

where C_v is the constant volume heat capacity (~1.2 MJm^{-3}K^{-1}) and v_p is the average phonon group velocity; note that this model provides some justification for the commonly assumed $\kappa^{-1} \propto L^{-1}$ dependence and offers additional physical meaning to the other constants computed during extrapolation. Using this method, we compute $\kappa = 2295 \pm 212$ Wm^{-1}K^{-1} at infinite length. Previous estimations of κ both in simulations and experiments have varied widely between 1000 and 4000 Wm^{-1}K^{-1} [7,25–27]. Although the variability of κ in the literature remains a subject of debate, we can use our estimated value to compare the relative influence of the substrate effect due to h-BN layers on κ.

For the cross-plane phonon transport, we similarly compute the G between bilayer graphene sheets as a reference for comparison. Using an effective C_v of 0.61 MJ/m^{3}K for two sheets, we find that G is 4.10 ± 1.43 MW/m^{2}K (and thermal relaxation time τ is 50 ± 17 ps). This value is comparable to that experimentally measured for the graphene/h-BN interface [4] while it is orders of magnitude lower than that of graphene with metal contacts [28,29].
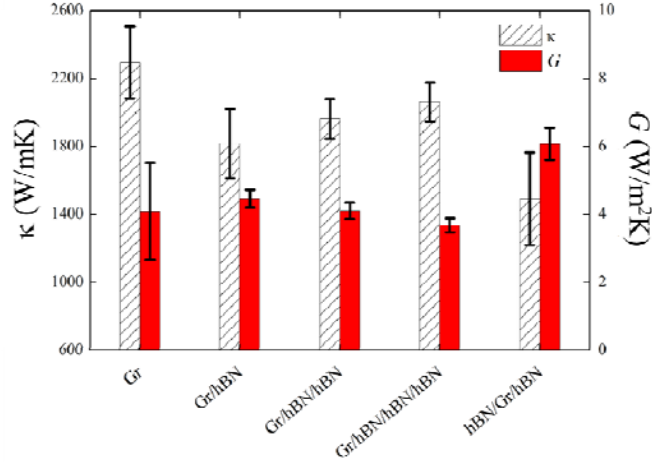
Figure 4. (a) Thermal conductivity (κ) and thermal conductance (G) of the listed systems at 300 K; the vertical bars represent the standard error.

Figure 4 shows the dependence of κ and G on the heterostructure composition. First, it is clear that κ is reduced to 1818 ± 205 Wm^{-1}K^{-1} once supported on monolayer h-BN – a 20% decrease from suspended graphene. The corresponding G is 4.5 ± 0.3 MWm^{-2}K^{-1}, which is comparable to that of bilayer graphene and within the computed standard error. The predicted suppression in κ is noticeably mitigated compared to conventional a-SiO$_2$ substrates with κ ≈ 600 Wm^{-1}K^{-1} [30]. The primary difference between the two cases is the exacerbation of σ|f$_{ad}$| in the latter case due to the presence of an atomically rough a-SiO$_2$ surface to which graphene conforms. We therefore attribute the larger κ of Gr/hBN to the vastly reduced σ|f$_{ad}$| resulting from the graphene sheet conformation to an atomically smooth surface. Interestingly, when we use previously parameterized LJ parameters for graphene and h-BN (which has inherently weaker interlayer binding as shown in Fig. S2 [15]), we compute a larger suppression of κ (Fig. S5 [15]). This suggests that the polarization-induced strength of the interlayer interactions is necessary to maintain such large values of κ, which we will further explore below.

The most interesting feature of Figure 4 is the predicted enhancement of κ with additional h-BN layers. For example, we compute a κ of 2062 ± 115 Wm^{-1}K^{-1} with the use of 3 h-BN layers (Gr/hBN/hBN/hBN) which is only 10% smaller than that of suspended graphene (and 13% larger than that of Gr/hBN). At the same time, G tends to diminish as the number of h-BN layers increases, which supports previous suggestions [31] that substrate-induced suppressions of κ are proportional to the degree of cross-plane phonon leakage. Furthermore, the final case of

encapsulated graphene by h-BN (hBN/Gr/hBN) is found to suppress κ to 1491 ± 274 W/mK while G increases to 6.1 ± 0.5 MW/m²K (note that this G is effectively double that of a single interface). All of these results are remarkably consistent with the predicted trend in κ following the inverse trend (or direct trend in the case of G) predicted for the variation in forces discussed above. This further supports the hypothesis that reducing the force variation throughout graphene can improve (suppress) the in-plane (cross-plane) thermal transport of supported graphene.
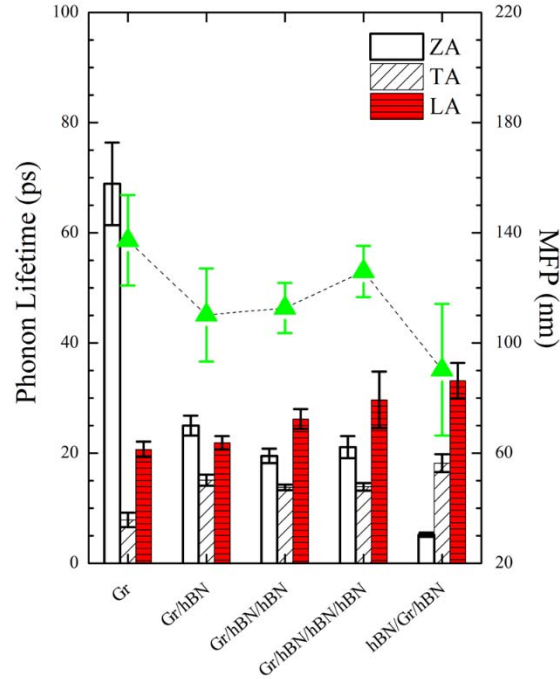

Figure 5. Comparison between the listed graphene/h-BN heterostructures of the (right) phonon lifetimes for the three acoustic modes at $k = (2/11)[2\pi/a_1, 2\pi/a_2]$ extracted from spectral energy density analysis and (left) effective total mean free path (MFP) of phonons from Equation 4. The k-point was chosen to be close enough to the Brillouin Zone center to sample acoustic branches with high group velocity while being far enough to clearly distinguish the three branches. The up-shift in phonon mode frequency compared to the graphene case was less than 7% for the ZA branch and less than 2% for the TA/LA branches.

To understand the origins of this behavior, we estimate the effective l_{MFP} of phonons in graphene for each case using the model described in Eq. 4 and depicted in Figure 5. Using this model, we find that $l_{MFP} \approx 140$ nm (with $v_p \approx 14$ km/s) in the case of free-standing graphene; although Ref. [24] approximates an experimental l_{MFP} of 775 nm using a similar model, their reported value is larger owing to a significantly larger κ around 4100 W/mK and slightly smaller

approximate values for C_V and v_p. Nonetheless, our model predicts that the trend in κ directly follows the change in l_{MFP} given that v_p is observed to be nearly constant throughout each case (Figure S6 [15]). To confirm that v_p should remain uninfluenced, we compute the phonon dispersion profiles and find that they remain virtually the same in all cases (Figure S7 [15]). Therefore, our findings to this point suggest that increasing the variation of forces throughout graphene effectively reduces l_{MFP} and ultimately decreases κ and increases G.

We can further elucidate the phonon transport behavior by approximating the phonon lifetimes of the acoustic modes using the spectral energy density (SED) method [32]. Here, the normal mode amplitudes are computed from classical MD and therefore include the full temperature-dependent anharmonicity; we should note that we are primarily interested in the relative phonon lifetime trends as explicit magnitudes can be inaccurate due to the single mode approximation [33]. Figure 5 shows the computed phonon lifetimes for the three acoustic modes – the out-of-plane ZA and two in-plane TA and LA modes – at a chosen k-point along the Γ-K direction for each heterostructure; owing to the much larger v_p and lifetimes of the acoustic modes compared to the optical modes, an analysis of the acoustic modes is sufficient to qualitatively understand the overall thermal transport behavior. First, in the case of graphene, our calculations predict considerably longer lifetimes for this particular ZA mode (~70 ps) compared to the corresponding LA and TA modes, which is consistent with previous theoretical results that attribute the large κ of suspended graphene to the flexural modes [26]. Once supported on monolayer h-BN, the ZA mode lifetime is estimated to decrease significantly to around 25 ps. In contrast, the lifetimes of the LA and TA modes are predicted to increase. Nonetheless, we can attribute the observed reduction of κ in the Gr/hBN case to the significant suppression of the ZA mode lifetime. Interestingly, the ZA mode lifetimes only slightly change as additional h-BN layers are added. However, the lifetimes of the TA and LA modes appear to continuously increase as additional h-BN layers are added; the enhancement of these in-plane modes can explain our observed increase in κ and l_{MFP}. Finally, in the hBN/Gr/hBN case, the observed decrease in κ follows from a further substantial reduction in the ZA mode lifetime despite the enhancement of the TA/LA mode lifetimes.

It is quite intuitive to understand the thermal transport with respect to the contributions from the out-of-plane and in-plane phonon modes given the two-dimensional nature of graphene. In Figure 6, we probe the relationship between the lifetimes of these modes and the standard

deviation of the total acting forces per carbon atom in the out-of-plane ($\sigma|f_z|$) and in-plane ($\sigma|f_{xy}|$) directions. Expectedly, our simulations reveal a distinct inverse relationship between the ZA mode lifetime and $\sigma|f_z|$, which dramatically increases when graphene is encapsulated by h-BN sheets, while seemingly uninfluenced by $\sigma|f_{xy}|$. Physically, one could imagine that the greater irregularity of the forces perpendicular to graphene disrupt possible collective flexural motions. On the other hand, the LA/TA mode lifetimes are inversely dependent upon $\sigma|f_{xy}|$, which decreases as the graphene sheet becomes increasingly flat with additional h-BN support, while seemingly independent of $\sigma|f_z|$; the in-plane vibrational motions become increasingly unhindered as the graphene sheet becomes flatter. This suggests that one possible route to enhance the thermal transport in supported graphene is to minimize the variation of strain throughout the sheet. In a perfectly flat configuration, the in-plane LA and TA modes may completely dominate heat transport, unlike the suspended graphene case in which the thermally-induced flexural ripples likely dominate heat transport. As a proof of concept, we consider the κ of graphene supported on and encapsulated in perfectly stiff mono-layer h-BN; in the absence of rippling throughout the substrate, graphene can achieve a nearly planar configuration due to the strong interlayer adhesion. We compute κ to be 2436 ± 294 W/mK and 2301 ± 107 W/mK, respectively, which suggests that supported graphene can acquire thermal transport properties comparable to suspended graphene, or potentially greater.
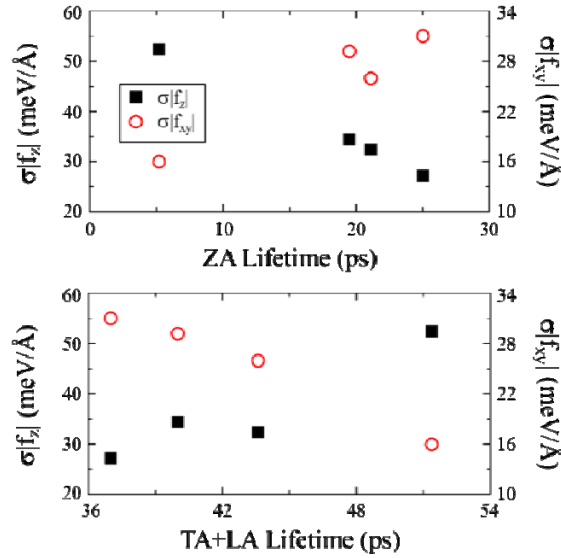

Figure 6. Comparison between the (a) out-of-plane ZA and (b) combined in-plane TA and LA phonon lifetimes to the variance of the atomic forces experienced by the graphene sheet in the out-of-plane ($\sigma|f_z|$) and in-plane ($\sigma|f_{xy}|$) directions.

Computational Methods

Optimization of interatomic interactions – To study the thermal transport in Gr/h-BN heterostructures, the intra- and inter-atomic interactions were described using classical force fields within a molecular dynamics framework. The Tersoff bond-order potential is commonly used in thermal transport simulations when sufficiently parameterized to reproduce the phonon dispersion behavior, especially for acoustic phonon modes near the Brillouin zone center. Here, the optimized parameters from Lindsay and Broido [9] and Sevik and coworkers [21] were used for graphene and h-BN sheets, respectively.

The interlayer interactions between graphene and h-BN were optimized to reproduce the energy predicted from semi-empirical dispersion corrected DFT using the method of Grimme [34] (so-called DFT-D2) based on the GGA-PBE functional [35] as implemented in the Vienna Ab Initio Simulation Package (VASP) [36]; the projected augmented wave (PAW) method [37] was used to describe the interaction between core and valence electrons with a planewave basis set using a kinetic energy cutoff of 450 eV. The training sets were constructed from three different stacking orientations by varying the interlayer separation distance. Here, a lattice constant of a = 2.488 Å was used, corresponding to 0.9% tensile (compressive) strain for graphene (h-BN). All training set calculations were performed using a periodic 3×3 hexagonal unit cell with vacuum spacing of 30 Å in the perpendicular direction to avoid interactions with the periodic images; a 6×6 Monkhorst-Pack k-point mesh [38] was used to sample the Brillouin zone. The three stacking orientations are denoted as AA, AB_B, and AB_N in which the subscript denotes the h-BN atom that is eclipsed by the adjacent C atom, as depicted in Fig. 1(a).

The classical Mie potential was optimized to emulate the graphene/h-BN binding energies from DFT-D2 through minimization of the cross-validation error objective function (δ):

$$\delta = \sqrt{\frac{1}{N} \sum_{n=1}^{N} (E_{DFT-D2}^n - E_{Mie}^n)^2}$$

where E_{DFT-D2}^n and E_{Mie}^n refer to the DFT-D2 and Mie potential energies, respectively, for the nth of N training sets. The interlayer interactions between h-BN sheets were described using the LJ potential from Neek-Amal and coworkers [22].

In-plane thermal conductivity – To calculate the κ at 300 K, we prepared each graphene/h-BN system with four different lengths (L = 94.9, 189.9, 284.8 and 379.8 nm) and width 7.97 nm corresponding to a (220, 440, 660, 880)×32 rectangular supercell; here, we use a lattice constant of 2.492 Å, which is optimized from the graphene Tersoff potential and resulted in 0.2% compressive strain for h-BN. Periodic boundary conditions were employed in all three directions with 10 nm of vacuum space included in the vertical direction to ensure no interactions with the periodic image.

To obtain the κ at each L, we performed 10 independent reverse non-equilibrium MD (RNEMD) simulations [39] with different initial velocity distributions for statistical accuracy. Each system was equilibrated for 500 ps within the canonical (NVT) ensemble using a Nosé-Hoover thermostat [40] with damping factor 1 ps and followed by 1 ns within the microcanonical (NVE) ensemble while imposing a heat flux through graphene with a velocity swap interval of 50 fs; here, all MD simulations adopted a 0.5 fs timestep and implemented using the LAMMPS package [41]. The temperature profile was extracted every 5 ps and the κ was computed from the average gradient of the linear region of the profile between the heat source and sink. Since the Debye temperature of graphene is above 2000 K [42], we included the quantum correction factor according to the procedure shown in Ref. [43]. The κ at infinite length was then extrapolated from $1/L$ vs $1/\kappa$ in which the thickness of graphene is assumed to be 0.335 nm (Figure S8 [15]); such a treatment is necessary as the phonon mean free path of free-standing graphene has previously been estimated to be ~775 nm [24], which is much larger than the simulation domain.

Cross-plane thermal conductance – To calculate G at 300 K, we prepared each graphene/h-BN system using a 115×115 hexagonal supercell, which we have extensively tested to be large enough to achieve convergence in G. Each system was equilibrated for 100 ps within the NVT ensemble using a Nosé-Hoover thermostat with damping factor 1 ps and 0.5 fs timestep. Then, a thermal pulse was applied to graphene (h-BN stack) at 330 K (270 K) for 1 ps using a Nosé-Hooever thermostat with damping factor 50 fs, followed by 500 ps of thermal relaxation within the NVE ensemble; this initial temperature gradient was found to be sufficient to maintain well-converged statistics. The temperature of each sheet was extracted every 50 fs; the difference in temperature was fit to an exponential and used to compute the thermal relaxation time (Figure S9 [15]). All results were averaged over 10 independent simulations with different initial velocity

distributions. Due to the 2D nature of each material, the interface can be modeled as a lumped capacitor [44] from which G can be approximated by

$$G = \frac{C_{v,eff}}{\tau}$$

where τ is the thermal relaxation time and $C_{v,eff}$ is the effective heat capacity $(= [1/(dC_{v,Gr}) + 1/(ndC_{v,hBN})]^{-1}$ where d is the layer thickness, 3.35 Å, and n is the number of h-BN layers). For all heat capacity calculations, the Debye approximation for 2D crystals in the low temperature limit was found to be reasonable $(C_v = 18[N/V]k_B[T/\Theta]^2I)$ with the Debye temperature (Θ) of graphene and h-BN assumed to be 2100 and 400 K, respectively.

Spectral energy density calculations and energetics − To compute the heterostructure energetics/forces and phonon lifetimes, the same 115×115 hexagonal supercells were used after equilibration at 300 K within the NVT ensemble. Forces and atomic velocities were extracted every 10 fs from 1 ns production runs with 0.5 fs timesteps; results for each system were averaged over 5 independent runs with different initial velocity distributions. The spectral energy density was computed using the procedure described in Ref. [32] at $k = (2/11)[2\pi/a_1, 2\pi/a_2]$ which was chosen to be close enough to the Brillouin Zone center to distinctly sample the acoustic branches while they maintained a large group velocity; the phonon frequency modes were found to up-shift slightly (by 7% for the ZA modes and 2% for the TA/LA modes). Peaks (Figure S10 [15]) were fit using Fityk [45].

Conclusions

In this work, the thermal conductivity (κ) and interfacial thermal conductance (G) of graphene supported with few-layer h-BN sheets (*i.e.*, monolayer, bilayer, trilayer, and encapsulated h-BN) was investigated using a combined density functional theory (DFT) and classical molecular dynamics (MD) approach. Using DFT, we first studied the nature of the interlayer interactions between graphene and h-BN. Our DFT simulations demonstrated that the h-BN sheets induce sub-lattice charge polarization along the graphene lattice, which in turn promotes strong interfacial adhesion particularly in the optimal AB$_B$ stacking configuration. Due to the deficiencies in the standard 12-6 Lennard Jones potential, parameters for the Mie potential

were optimized to describe the interlayer interactions. MD simulations were then performed to evaluate the κ and G of graphene supported on few-layer h-BN. In transitioning from fully suspended to supported on mono-layer h-BN, κ is reduced from around 2300 to 1800 $Wm^{-1}K^{-1}$, which is still much larger than that of graphene on amorphous SiO_2 ($\cong$ 600 $Wm^{-1}K^{-1}$), and G is around 4.5 $MWm^{-2}K^{-1}$. Interestingly, κ and the overall thermal transport anisotropy (*i.e.*, κ / G) increases as the number of h-BN support layers increases. Our analysis revealed that the increased thermal conductivity is driven by the enhanced lifetime of the in-plane LA and TA acoustic phonon modes while the ZA mode lifetime is suppressed, which in turn is possible due to the strong adhesion between graphene and h-BN and the resultant flattening of the sheets in the heterostructure to minimize the fluctuations in the internal strain forces. These findings suggest that one possible route to enhance the thermal transport in supported graphene is to bolster the lifetimes of the in-plane phonon modes by minimizing the local variation of forces throughout the graphene sheet. In fact, our results highlight the potential to go beyond the thermal transport limits of suspended graphene using such a strategy, which may be ideal for thermal management in nanoelectronic devices.

On a final note, it is evident that much of the physics of phonon transport in layered materials remains unclear. However, the systematic computational framework presented here may be useful for the exploration of other graphene and layered dielectric material heterostructures, in addition to structural factors including polycrystallinity, lattice strain, and Moiré patterns. In particular, the variation of the forces along the graphene sheet can be an intuitive physical descriptor to understand phonon transport. Yet, future investigations of the relative contributions of the in-plane and cross-plane phonon modes may require better descriptions of both the interlayer non-bonding interactions and the bonding forces throughout each sheet. In particular, it may be worthwhile to explore quantum mechanical descriptions of weak noncovalent interactions that are more rigorous than the semi-empirical Grimme corrections to dispersion used here. We anticipate that this work can serve as motivation to develop more robust computational methods to explore in-depth the thermal transport of layered-material heterostructures.

Acknowledgments

Supporting Information

Additional data is available describing the influence of additional h-BN layers on polarization, the binding energies and thermal conductivity using a 12-6 LJ potential, pair distribution functions, phonon group velocities, phonon dispersion profiles, and representative simulation data used to extract thermal conductivity, thermal relaxation times, and phonon mode-specific lifetimes.

References

[1]   K.C. Yung, W.M. Wu, M.P. Pierpoint, F.V. Kusmartsev, Introduction to graphene electronics – a new era of digital transistors and devices, Contemp. Phys. **54**, 233–251 (2013).

[2]   C.R. Dean, A.F. Young, I. Meric, C. Lee, L. Wang, S. Sorgenfrei, K. Watanabe, T. Taniguchi, P. Kim, K.L. Shepard, J. Hone, Boron nitride substrates for high-quality graphene electronics., Nat. Nanotechnol. **5**, 722–6 (2010).

[3]   J. Lee, H.Y. Chang, T.J. Ha, H. Li, R.S. Ruoff, A. Dodabalapur, D. Akinwande, High-performance flexible nanoelectronics: 2D atomic channel materials for low-power digital and high-frequency analog devices, Tech. Dig. - Int. Electron Devices Meet. 491–494 (2013).

[4]   C.C. Chen, Z. Li, L. Shi, S.B. Cronin, Thermal interface conductance across a graphene/hexagonal boron nitride heterojunction, Appl. Phys. Lett. **104**, 081908 (2014).

[5]   X. Wang, T. Huang, S. Lu, High performance of the thermal transport in graphene supported on hexagonal boron nitride, Appl. Phys. Express. **6**, 075202 (2013).

[6]   J. Zhang, Y. Hong, Y. Yue, Thermal transport across graphene and single layer hexagonal boron nitride, J. Appl. Phys. **117**, 134307 (2015).

[7]   B. Kong, S. Paul, M. Nardelli, K. Kim, First-principles analysis of lattice thermal conductivity in monolayer and bilayer graphene, Phys. Rev. B **80**, 033406 (2009).

[8]   N. Mounet, N. Marzari, First-principles determination of the structural, vibrational and thermodynamic properties of diamond, graphite, and derivatives, Phys. Rev. B **71**, 205214 (2005).

[9]   L. Lindsay, D.A. Broido, Optimized Tersoff and Brenner empirical potential parameters for lattice dynamics and phonon thermal transport in carbon nanotubes and graphene, Phys. Rev. B **81**, 205441 (2010).

[10]   Y. Wang, A.K. Vallabhaneni, B. Qiu, X. Ruan, Two-dimensional thermal transport in graphene: A review of numerical modeling studies, Nanosc. Microsc. Therm. **18**, 155–182 (2014).

[11]   O. Hod, Graphite and hexagonal boron-nitride have the same interlayer distance. Why?, J. Chem. Theory Comput. **8**, 1360–1369 (2012).

[12]   G. Giovannetti, P. Khomyakov, G. Brocks, P. Kelly, J. van den Brink, Substrate-induced band gap in graphene on hexagonal boron nitride: Ab initio density functional calculations, Phys. Rev. B **76**, 073103 (2007).

[13]   B. Sachs, T.O. Wehling, M.I. Katsnelson, A.I. Lichtenstein, Adhesion and electronic structure of graphene on hexagonal boron nitride substrates, Phys. Rev. B **84** 195414 (2011).

[14]   Y. Fan, M. Zhao, Z. Wang, X. Zhang, H. Zhang, Tunable electronic structures of graphene/boron nitride heterobilayers, Appl. Phys. Lett. **98**, 083103 (2011).

[15]   See Supplemental Material at [URL] for data that describes the influence of additional h-BN layers on polarization, the binding energies and thermal conductivity using a 12-6 LJ potential, pair distribution functions, phonon group velocities, phonon dispersion profiles, and representative simulation data used to extract thermal conductivity, thermal relaxation times, and phonon mode-specific lifetimes.

[16]   J. Lahiri, T. S Miller, A. J Ross, L. Adamska, I.I. Oleynik, M. Batzill, Graphene growth and stability at nickel surfaces, New J. Phys. **13**, 025001 (2011).

[17] Z. Cao, P. Wang, W. Gao, L. Tao, J.W. Suk, R.S. Ruoff, D. Akinwande, R. Huang, K.M. Liechti, A blister test for interfacial adhesion of large-scale transferred graphene, Carbon **69**, 390–400 (2014).

[18] Z. Xu, M.J. Buehler, Interface structure and mechanics between graphene and metal substrates: a first-principles study., J. Phys. Condens. Matter. **22**, 485301 (2010).

[19] G. Constantinescu, A. Kuc, T. Heine, Stacking in bulk and bilayer hexagonal boron nitride, Phys. Rev. Lett. **111**, 036104 (2013).

[20] W. Gao, A. Tkatchenko, Sliding mechanisms in multilayered hexagonal boron nitride and graphene: The effects of directionality, thickness, and sliding constraints, Phys. Rev. Lett. **114**, 096101 (2015).

[21] C. Sevik, A. Kinaci, J.B. Haskins, T. Çağın, Characterization of thermal transport in low-dimensional boron nitride nanostructures, Phys. Rev. B **84**, 085409 (2011).

[22] M. Neek-Amal, F.M. Peeters, Graphene on boron-nitride: Moiré pattern in the van der Waals energy, Appl. Phys. Lett. **104**, 041909 (2014).

[23] S.K. Singh, M. Neek-Amal, S. Costamagna, F.M. Peeters, Thermomechanical properties of a single hexagonal boron nitride sheet, Phys. Rev. B **87**, 184106 (2013).

[24] S. Ghosh, I. Calizo, D. Teweldebrhan, E.P. Pokatilov, D.L. Nika, A.A. Balandin, W. Bao, F. Miao, C.N. Lau, Extremely high thermal conductivity of graphene: Prospects for thermal management applications in nanoelectronic circuits, Appl. Phys. Lett. **92**, 151911 (2008).

[25] W. Cai, A.L. Moore, Y. Zhu, X. Li, S. Chen, L. Shi, R.S. Ruoff, Thermal transport in suspended and supported monolayer graphene grown by chemical vapor deposition, Nano Lett. **10**, 1645–51 (2010).

[26] L. Lindsay, D.A. Broido, N. Mingo, Flexural phonons and thermal transport in graphene, Phys. Rev. B **82**, 115427 (2010).

[27] A.A. Balandin, Thermal properties of graphene and nanostructured carbon materials., Nat. Mater. **10**, 569–581 (2011).

[28] K.F. Mak, C.H. Lui, T.F. Heinz, Measurement of the thermal conductance of the graphene/SiO_2 interface, Appl. Phys. Lett. **97**, 221904 (2010).

[29] Y.K. Koh, M.H. Bae, D.G. Cahill, E. Pop, Heat conduction across monolayer and few-layer graphenes, Nano Lett. **10**, 4363–4368 (2010).

[30] J.H. Seol, I. Jo, A.L. Moore, L. Lindsay, Z.H. Aitken, M.T. Pettes, X. Li, Z. Yao, R. Huang, D. Broido, N. Mingo, R.S. Ruoff, L. Shi, Two-dimensional phonon transport in supported graphene, Science **328**, 213–6 (2010).

[31] M.M. Sadeghi, I. Jo, L. Shi, Phonon-interface scattering in multilayer graphene on an amorphous support., Proc. Natl. Acad. Sci. **110**, 16321–6 (2013).

[32] J.A. Thomas, J.E. Turney, R.M. Iutzi, C.H. Amon, A.J.H. McGaughey, Predicting phonon dispersion relations and lifetimes from the spectral energy density, Phys. Rev. B **81**, 94303 (2010).

[33] Y. Lee, A.J. Pak, G.S. Hwang, What is the thermal conductivity limit of silicon germanium alloys?, Phys. Chem. Chem. Phys. **18**, 19544−19548 (2016).

[34] S. Grimme, Semiempirical GGA-type density functional constructed with a long-range dispersion correction, J. Comput. Chem. **27**, 1787–99 (2006).

[35] J.P. Perdew, K. Burke, M. Ernzerhof, Generalized gradient approximation made simple, Phys. Rev. Lett. **77**, 3865–3868 (1996).

[36] G. Kresse, J. Furthmüller, Efficient iterative schemes for ab initio total-energy

calculations using a plane-wave basis set, Phys. Rev. B **54**, 11169–11186 (1996).

[37]   P. Blöchl, Projector augmented-wave method, Phys. Rev. B **50**, 17953–79 (1994).

[38]   H.J. Monkhorst, J.D. Pack, Special points for Brillouin-Zone integrations, Phys. Rev. B **13**, 5188–5192 (1976).

[39]   F. Mu ller-Plathe, A simple nonequilibrium molecular dynamics method for calculating the thermal conductivity, J. Chem. Phys. **106**, 6082 (1997).

[40]   W. Hoover, Canonical dynamics: Equilibrium phase-space distributions, Phys. Rev. A **31**, 1695–7 (1985).

[41]   S. Plimpton, Fast parallel algorithms for short-range molecular dynamics, J. Comput. Phys. **117**, 1–19 (1995).

[42]   D.K. Efetov, P. Kim, Controlling electron-phonon interactions in graphene at ultrahigh carrier densities, Phys. Rev. Lett. **105**, 256805 (2010).

[43]   J.-W. Jiang, J. Lan, J.-S. Wang, B. Li, Isotopic effects on the thermal conductivity of graphene nanoribbons: Localization mechanism, J. Appl. Phys. **107**, 054314 (2010).

[44]   C.F. Carlborg, J. Shiomi, S. Maruyama, Thermal boundary resistance between single-walled carbon nanotubes and surrounding matrices, Phys. Rev. B **78**, 205406 (2008).

[45]   M. Wojdyr, Fityk: A general-purpose peak fitting program, J. Appl. Crystallogr. **43**, 1126–1128 (2010).